Forum Article

Key Parameters and Thresholds Values for Obtaining High Performance Perovskite Solar Cells Indoors from Full Br Compositional and Bandgap Engineering

Jie Xu, Suresh Kumar Podapangi, Sathy Harshavardhan Reddy, Luigi Angelo Castriotta, Aldo Di Carlo, and Thomas M. Brown*

Cite This: https://doi.org/10.1021/acsaem.2c03394

Read Online

ACCESS | Metrics & More | Article Recommendations | SI Supporting Information

ABSTRACT: Perovskite solar cells (PSCs) have different theoretical optimal bandgaps (E_g) for outdoor and indoor light harvesting due to the different spectral distributions of the sun and indoor lamps. This work focuses on understanding how both indoor and outdoor photovoltaic (PV) performance of $Cs_{0.05}(MA_{0.17}FA_{0.83})_{0.95}Pb(I_{1−x}Br_x)_3$ PSCs depend on $Br^−$ content (x) spanning the whole 0−100% range, not only efficiency but also stability. E_g increases linearly with x: $E_g/eV = 0.75x+1.48$. Cells with $x = 0.17$ delivered the highest efficiency under indoor illumination, which did not correspond to the optimal theoretical bandgap. Via in depth analysis of crystal structure, morphology, and optoelectronic properties, we propose five key parameters and associated threshold values to be surpassed that enable one to achieve indoor efficiencies greater than 25% (1000 lx). First, films should possess average grain sizes greater than 300 nm (i.e., grain sizes > 70% of film thickness) and intergrain spacing ≪ 10 nm. Additionally, On/Off dark current and shunt/series resistance ratios should be higher than 10^2. Lastly the ratio between current density under indoor illumination and recombination currents in the dark should be >10. The aging rate of cells measured indoors (a fall of 65%) was higher than under 1 sun (41% fall), indicating that device performance is more sensitive to defects arising upon aging when measured under low intensity indoor light. Our investigation provides key parameters that can become a useful tool for researchers aiming to develop improved PSCs for indoor applications.

KEYWORDS: perovskite solar cells, bandgap engineering, photovoltaic cells, indoor light harvesting, compositional engineering
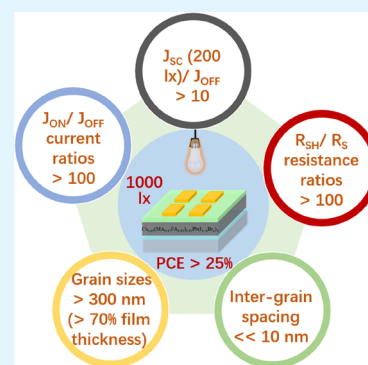
1. INTRODUCTION

Organic−inorganic halide perovskite solar cells (PSCs) have attracted widespread attention because of soaring photovoltaic (PV) performance now reaching 25.7% as well as low cost solution-based fabrication processes utilized.[1−4] In addition, PSCs have emerged as one of the most competitive candidates for indoor photovoltaics (IPVs) applications due to their tunable bandgap (E_g), good mechanical flexibility, low weight, and high power conversion efficiency (PCE), especially under low and artificial light conditions.[5−9]

Currently, with the swift development of the Internet of things (IoT), the demand for IPVs to power microelectronic indoor devices (e.g., sensors, wearable devices, and actuators) is high to reduce the need for batteries and connection to the electrical grid.[10−13] Extensive studies in PSCs have been carried out under standard test conditions (i.e., 1 sun illumination), whereas few studies have focused on indoor PV applications. Indoor light, also known as artificial or ambient light, is now typically generated by LEDs and fluorescent lamps (FLs). These light sources have a narrower wavelength range of the irradiance spectrum compared to sunlight.[9,14−16] Hence, the perovskite absorber for indoor light

conversion should have a wider E_g compared to those for applications under natural sunlight to reduce thermalization of photoexcited charge carriers.[17−20]

Recent initial studies have reported that the efficiency of PSCs for indoor light conversion can be improved by engineering the E_g of perovskite formulations.[21−23] Theoretical calculations by Freunek et al. have shown that the optimal E_g of PVs for indoor light harvesting is 1.9 eV.[17] Li et al. employed $(FA_{0.6}MA_{0.4})_{0.9}Cs_{0.1}Pb(I_{0.6}Br_{0.4})_3$ with an E_g of 1.75 eV and attained an indoor PCE (i-PCE) of 22.7% at 200 lx under LED.[16] Wu et al. adopted an $MA_{0.85}Cs_{0.15}Pb(I_{1−x}Br_x)_3$ perovskite layer with i-PCEs of 24.6% at 200 lx under LED (E_g ≈ 1.66 eV).[24] Feng's group designed a $CH_3NH_3PbI_{2−x}BrCl_x$ triple-anion perovskite with E_g ≈ 1.8 eV, achieving i-PCE of 36.2% at 1000 lx under FL.[19] However, as far as we know, He
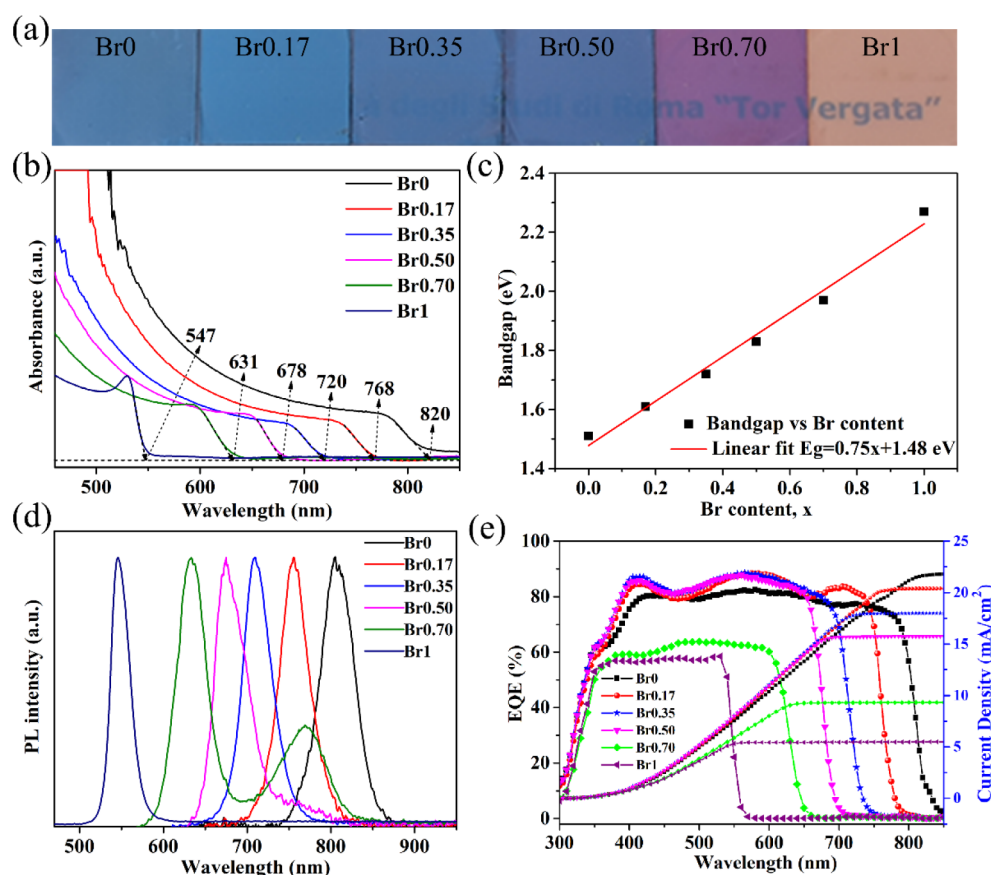
Figure 1. (a) Photographs, (b) absorption spectra, (c) linear relationship between bandgap (E_g) and Br^- content (x), and (d) normalized PL spectra of perovskite $Cs_{0.05}(MA_{0.17}FA_{0.83})_{0.95}Pb(I_{1-x}Br_x)_3$ [$0 \leq x \leq 100\%$] films. (e) External quantum efficiency (EQE) curves with integrated current densities for the best performing devices.

et al. achieved the record efficiency of 34.8% at 200 lx and 40.1% at 824 lx based on an $(FAPbI_3)_{0.97}(MAPbBr_3)_{0.03}$ perovskite with a narrow E_g of 1.59.[8] Therefore, in addition to the E_g, there are other more important factors affecting the indoor PV performance of PSCs.

To comprehensively explore the effect of E_g and perovskite film properties on the indoor and outdoor PV performances of PSCs, we systematically developed and investigated triple-cation PSCs with the content of Br^- ions varied over the full 0−100% range. We did not use any additives and interfacial layers that would further improve efficiency, because these would introduce more complex influencing factors. Our main aim is to further understand what are the key properties of the perovskite layer that affect efficiency, in particular under indoor lighting. We selected cesium-containing triple-cation PSCs in the ITO/SnO$_2$/Cs$_{0.05}$(MA$_{0.17}$FA$_{0.83}$)$_{0.95}$Pb(I$_{1-x}$Br$_x$)$_3$/Spiro-OMeTAD/Au architecture because they possess high efficiency as well as improved thermal stability and reproducibility.[25,26] By substituting I with Br from 0 to 100%, we were able to link PV performance under both 1 sun and indoor light conditions not only to the E_g, which varied from 1.5 to 2.3 eV, but also, crucially, to the optoelectronic and morphological properties of films. In fact, the latter dominate the influence on device performance compared to the bandgap value that would be theoretically more suitable. Importantly, we extended the systematic study, together with XRD analyses, to long-term stability, which is often overlooked in indoor studies. Our investigation has enabled us to unravel operation mechanisms in indoor PV and identify five important

parameters and the thresholds that need to be surpassed in order to achieve high performance at low light levels. These can become a useful tool for researchers aiming to develop improved PSCs for indoor applications.

2. RESULTS AND DISCUSSION

2.1. Bandgap Engineering with Different Br^- Content Ratios.
Figure 1a displays photographs of perovskite films $Cs_{0.05}(MA_{0.17}FA_{0.83})_{0.95}Pb(I_{1-x}Br_x)_3$ prepared with different Br^- contents ($0 \leq x \leq 100\%$). Ultraviolet−visible (UV−vis) absorption spectra show that the absorption edge blue shifts as the Br^- content increases from 0 to 100% (Figure 1b). The values of E_g were 1.51, 1.61, 1.72, 1.83, 1.97, and 2.27 eV for x of 0, 0.17, 0.35, 0.5, 0.7, and 1, respectively, as extracted from the onset of the absorption spectra. A linear dependence of E_g with Br^- content was observed (Figure 1c):

$$E_g/eV = 0.75x + 1.48 \tag{1}$$

We see the same behavior from the photoluminescence (Figure 1d) and external quantum efficiency (EQE) spectra (Figure 1e).[27−29] A new sub-bandgap peak and a low energy tail appear in the PL spectra of the Br0.7 and Br0.5 films, respectively. These features will be discussed in Section 2.5.

2.2. Photovoltaic Performance of Perovskite Solar Cells.
ITO/SnO$_2$/perovskite/Spiro-OMeTAD/Au architectures (Supporting Information Figure S1a) with different $Cs_{0.05}(MA_{0.17}FA_{0.83})_{0.95}Pb(I_{1-x}Br_x)_3$ [$0 \leq x \leq 100\%$] perovskite layers were investigated under both standard test
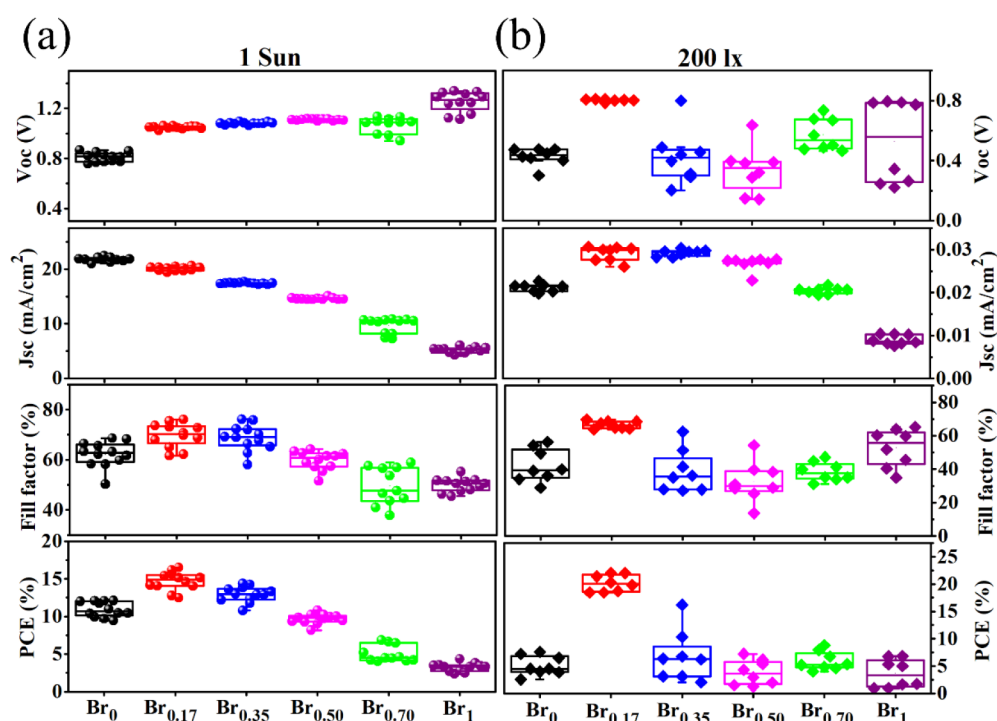
Figure 2. Photovoltaic parameters for the $Cs_{0.05}(MA_{0.17}FA_{0.83})_{0.95}Pb(I_{1-x}Br_x)_3$ [$0 \leq x \leq 100\%$] perovskite solar cells (PSCs) measured (a) under standard test conditions (STC, AM1.5G, 1000 W/m², 25 °C) and (b) under illumination from an LED lamp (OSRAM P25) at 200 lx.

conditions (STC, AM1.5G, 1000 W/m², 25 °C) and indoor LED illumination (irradiance plotted in Figure S1b).

Figure 2a and Table S1 present the PV parameters measured under STC. V_{OC} monotonically increases with Br⁻ contents, from 0.81 ± 0.04 V at $x = 0$ to 1.25 ± 0.08 V at $x = 1$; conversely J_{SC} decreases, from 21.8 ± 0.4 to 5.2 ± 0.5 mA/cm². The monotonic increasing trend of V_{OC} with x and thus E_g is consistent with the general expression for V_{OC} vs E_g:[30]

$$V_{OC} = \frac{kT}{q} \ln\left(\frac{I_L}{K_2}\right) + \frac{E_g}{q} \qquad (2)$$

Photocurrent behavior is explained by a diminished absorption of photons with increasing E_g:[31]

$$J_{SC} = q \int_0^\infty EQE(E) f_s(E) \, dE \qquad (3)$$

where $EQE(E)$ is the quantum efficiency and $f_s(E)$ is the solar photon flux. Because $EQE(E) = 0$ for all photon energies $E < E_g$, eq 3 can be written as

$$J_{SC} = q \int_{E_g}^\infty EQE(E) f_s(E) \, dE \qquad (4)$$

Clearly, the smaller E_g is, and for broad EQEs spanning up to the UV such as those delivered by PSCs, the more photons will be harvested leading to higher generated currents, J_{SC}.

The indoor V_{OC} and J_{SC} values do not show the same monotonic trends observed at STC (Figure 2b). The reason is that trap-state density plays a more important role under the much lower optical power densities found indoors of 0.77−3.85 W/m² (200−1000 lx) compared to those found at STC (1000 W/m²), with major effects on PCE.[19] The cell with the perovskite layer containing Br0.17 still remains the most efficient one. However, at these lux levels, the difference between Br0.17 and the other compositions was greatly

amplified. The average PCE at this composition was at least 50% higher than at other Br⁻ contents at 1000 lx (Figure S2), and the gap was even greater at the lower 200 lx (Figure 2b). At 200 lx the best, average, and stabilized PCEs were 22.0%, 20.4%, and 21.6%, respectively, for the Br 0.17 cell. At 1000 lx these values improved to 27.1%, 25.2%, and 26.2% (Figure S3 and Tables S2 and S3). For comparison, the champion device delivered a PCE of 16.5% at STC. We calculated the hysteresis index (HI), HI = $(PCE_{BW} − PCE_{FW})/PCE_{BW}$,[32] based on $J–V$ forward (FW) and backward (BW) scans (Figure S4). Although, there still is no consensus explanation in the literature, inverted (i.e., negative) hysteresis is likely a sign of significant movement of anions and cations toward the transport layers.[33,34] HI varies from 0.046 to 0.253 (Table S4). Notably, bromine-free (Br0) cell exhibits negligible hysteresis (0.046), the Br0.17 cell shows the smallest hysteresis (0.112) compared with other bromine-containing devices (HI ranging from 0.126 to 0.253). This high hysteresis is notorious in wide-bandgap Br-containing perovskites and can be limited by interfacial or additives engineering.[32,35,36]

PCEs of our experimental PV cells at STC and under LED light are plotted as a function of bandgap in Figure 3 together with the theoretical limits for single-junction solar cells (Shockley−Queisser limit/detailed balance limit).[37,38] The theoretical PCE at AM 1.5G shows a broad peak between 1.0 and 1.5 eV (with the maximum at 1.34 eV). Above this value the PCE decreases steadily with E_g. Our experimental data follow this trend above 1.6 eV due to lower photon harvesting capabilities of larger E_g. However, the measured PCE presents a maximum at 1.61 eV, ∼200−300 meV away from the theoretical peaks, suggesting that there are additional critical factors influencing performance in addition to E_g, which also explain the gap between the maximum values of experimental (maximum PCEs of 27.1% and 16.5% under LED and STC)
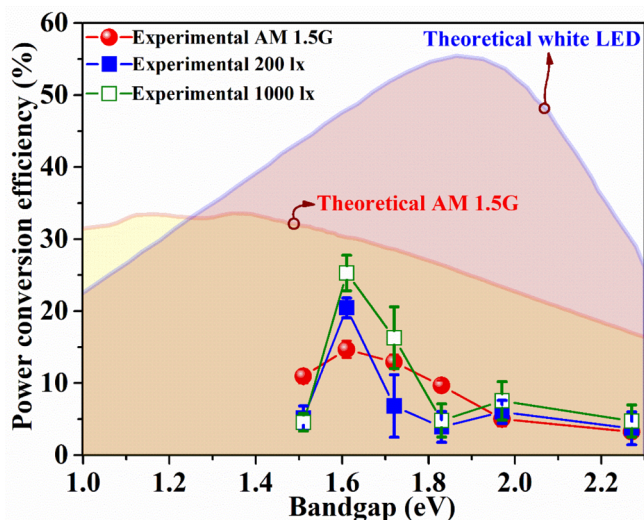
Figure 3. Theoretically maximum limit power conversion efficiency (PCE) for single-junction solar cells (Shockley−Queisser limit/detailed balance limit) at standard test conditions (STC, AM1.5G, 1000 W/m², 25 °C, red continuous line) and white LED (blue continuous line),[24,37] and the average PCE for our experimental devices at various of E_g measured under STC (red filled circles), at 200 lx (blue filled squares), and at 1000 lx (green empty squares).

and ideal cells (maximum PCEs of 56% at 1.89 eV for LEDs and 33% at 1.34 eV at STC).[24,37]

2.3. Morphologies and Properties of Perovskite Films. Figure 4 shows the X-ray diffraction (XRD) patterns (Figure 4a) and top-view scanning electron microscope images (Figure 4b) and the grain size (d_G) distribution of perovskite films (Figure 4c), for each Br⁻ content. XRD spectra (Figure 4a) show that the main peaks are displaced toward larger values of 2θ with an increasing amount of bromide, since smaller Br⁻ [ionic radius (IR) = 1.96 Å] ions are substituting the larger I⁻ ions (IR = 2.2 Å).[29,39,40] This displacement has been attributed to changes in the crystal structure, i.e., a gradual shift from the tetragonal phase of pure CsMAFAPbI₃ to the cubic phase of pure CsMAFAPbBr₃.[41,42]

SEM images tell us that from $x = 0$ ($d_G = 270 \pm 55$ nm) to $x = 0.5$ ($d_G = 300 \pm 54$ nm), it is the Br0.17 perovskite film that has the larger average grain size ($d_G = 324 \pm 57$ nm), explaining, together with it being more compact, its better PV performance when used in a solar cell. For $x = 0.7$ ($d_G = 425 \pm 114$ nm) and 1 ($d_G = 454 \pm 122$ nm), grain sizes were the largest. The standard deviation of over 100 nm (evaluated over 30 grains) was more than double that of grain sizes in the Br0 to Br0.5 range (~50 ± 10 nm), indicating less reproducible film forming morphologies for the higher Br range, and visible gaps/cracks appeared at the grain boundaries (highlighted with red squares in Figure 4b). These were estimated to be 28 ± 4.7 and 24 ± 2.6 nm wide (over ten measurements) for Br0.7 and Br1 films, leading to increased charge recombination and poor indoor PV performance (Figure 2).[43] Notably, the intergrain spacing for other perovskite films ($x \leq 0.5$) are not measurable with the software and thus well below 10 nm. In summary, considering that the average thickness of the perovskite films cast in all our devices was 440 ± 20 nm (Figure S5), morphological analysis indicated that for achieving high PCEs (>25%) under low intensity indoor light, films with average grain sizes exceeding 300 nm, corresponding to more than 70% of film thickness, and high compactness with intergrain spacing

≪ 10 nm (summarized in Table 1) must be obtained. These characteristics reduce grain boundaries and limit defect sites and shunting paths that would provide a channel for undesirable charge recombination.[44]

Figure 5 in fact confirms this picture. The Off current (J_{OFF}, dark current densities at −1 V, 8.9 × 10⁻⁴ mA cm⁻²) of the Br0.17 cell is almost an order of magnitude lower than those of all other devices, indicating a lower charge carrier recombination in the cell (Figure 5a).[45−47] Figure 5b shows clearly that the PCE follows closely the J_{ON}/J_{OFF} current ratio (ratio between the dark current densities at +1 and −1 V). This was 6.9 × 10² for the Br0.17 cell, at least an order of magnitude greater than those in all other cases (difference mainly determined by the respective recombination currents) (Table S5). In this context, we calculated the ratio between J_{SC} at 200 lx and J_{OFF} [J_{SC} (200 lx) /J_{OFF}] and in Figure 5c we show that it has a strong bearing on the PCE values obtained. In fact, it is only the Br0.17 cell for which this ratio is greater than 10 (i.e., it is 35). The latter parameter, with the corresponding threshold value that enables reaching high efficiencies indoors, is included in Table 1 together with the others.

Series resistance (R_S), shunt resistance (R_{SH}), and R_{SH}/R_S extracted from the J−V curves of the cells under STC are summarized in Figure 5d and Figure S6. The Br0.17 devices delivered the lowest R_S (6.6 ± 0.5 Ω·cm²) compared to those with different Br⁻ content (8.6−52.4 Ω·cm²), leading to better FF and charge extraction (Figure S6).[48,49] We also found a strong correlation between V_{OC} values indoors and R_{SH} (Figure S7). Br0.17 devices exhibited the largest R_{SH} (0.90 ± 0.13 kΩ·cm²) compared to other Br⁻ content devices, which fell in the 0.43−0.72 kΩ·cm² range. A high R_{SH} results from a more uniform better quality perovskite film,[50,51] which is paramount at low light levels found indoors. Figure 5d plots PCE vs R_{SH}/R_S ratio (to combine the effect of both resistances): the correlation between the two is very strong. Br0.17 cells were the only devices with R_{SH}/R_S ratios (128 ± 16) greater than 100, possessing a beneficially high R_{SH} and low R_S at the same time. The correlation is so strong that we suggest the R_{SH}/R_S ratio as a new key parameter to identify thresholds that determine high performance indoors and is included in Table 1.

2.4. Stabilities of the Devices. We probed the long-term stability of unencapsulated PSCs in an ambient atmosphere in the dark according to the ISOS-D-1 protocol (dark storage, ambient air, 23 ± 4 °C).[52,53] Figure 6a shows the evolution in time of the PCEs measured at STC. Although there is statistical overlap in the data for devices with different Br composition, both the average and the best less degraded cells belonged to Br0.17 cells. In fact, Br0.17 devices maintained 74% of the original average PCE after 50 days of storage. The PCE of Br0.35, Br0.7, and Br1 cells had the most significant drop (below 66% of their initial values) (Figure 6b). Decomposition is also apparent from the color change of the films (Figure 6d). As noted previously, the films which degrade faster typically have smaller grain sizes and/or wider intergrain spacing, making the films more prone to diffusion and reaction with moisture leading to faster decomposition and degradation.[54,55] XRD characterization at this time (Figure 6c) shows that the intensity ratio of PbI₂/(100) diffraction peak increased from 2.3 to 4.1 for the Br0 film, a symptom of material decomposition from α-phase perovskite to PbI₂.[56] No PbI₂ peaks were visible for other Br⁻ compositions. The new peaks
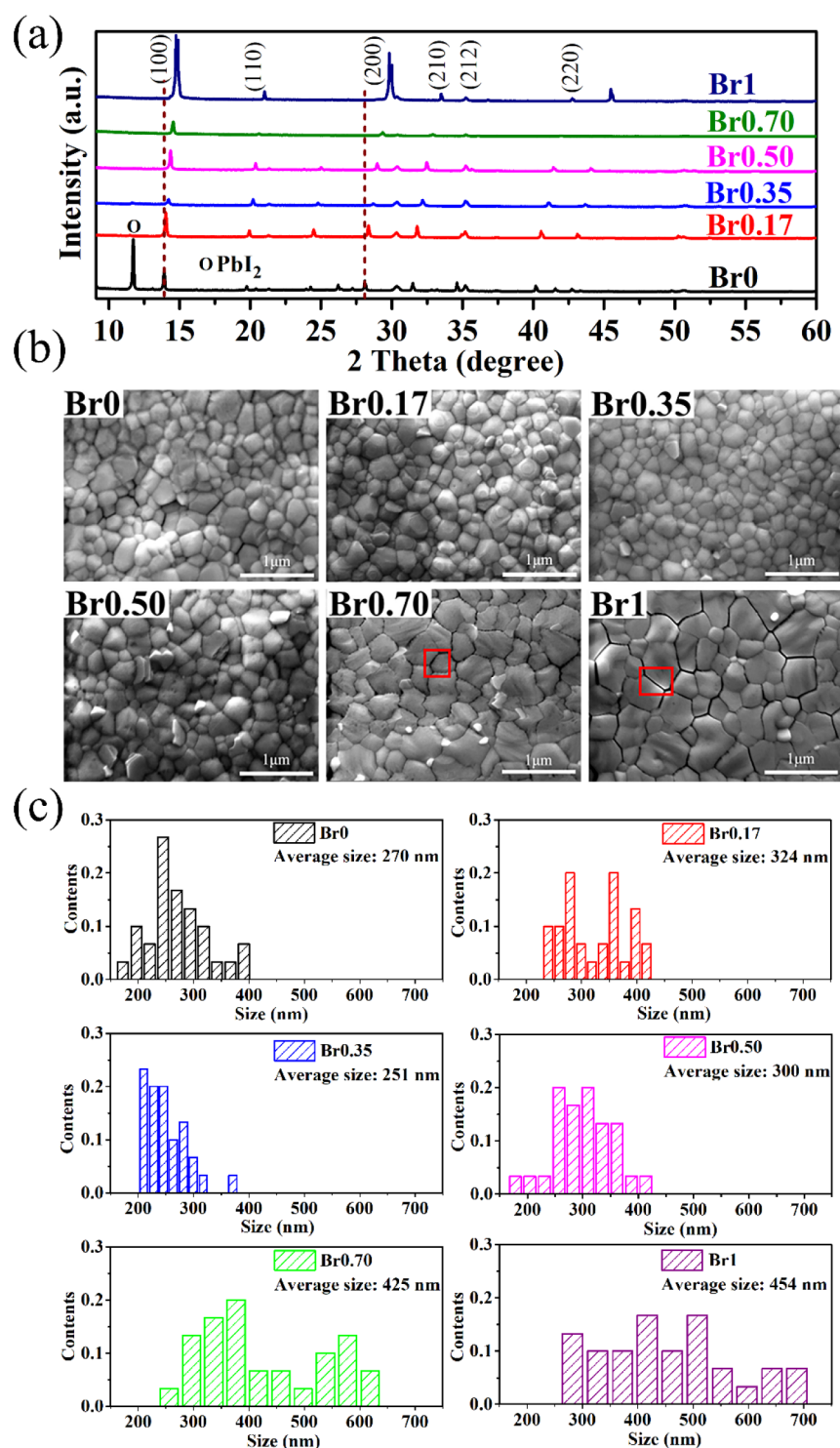
Figure 4. (a) XRD patterns of perovskite films $Cs_{0.05}(MA_{0.17}FA_{0.83})_{0.95}Pb(I_{1-x}Br_x)_3$ $[0 \leq x \leq 100\%]$. (b) Top-view scanning electron microscope images. Gaps/cracks at the grain boundaries were marked with the red square. (c) Statistical histogram distribution of crystal grain sizes of the perovskite films $Cs_{0.05}(MA_{0.17}FA_{0.83})_{0.95}Pb(I_{1-x}Br_x)_3$ $[0 \leq x \leq 100\%]$.

Table 1. Key Parameters and Their Threshold Values That Enabled Achievement of High $[25\%$ $(1000$ lx$)$ and 20% $(200$ lx$)]$ Power Conversion Efficiency under Low Levels Indoors for Triple-Cation $ITO/SnO_2/Cs_{0.05}(MA_{0.17}FA_{0.83})_{0.95}Pb(I_{1-x}Br_x)_3/$ Spiro-OMeTAD/Au Solar Cells

Key parameters	Average grain sizes	Intergrain spacing	J_{ON}/J_{OFF} current ratio	J_{SC} (200 lx)/J_{OFF}	R_{SH}/R_S resistance ratio
Threshold values	>300 nm (>70% of film thickness)	≪10 nm	>100	>10	>100
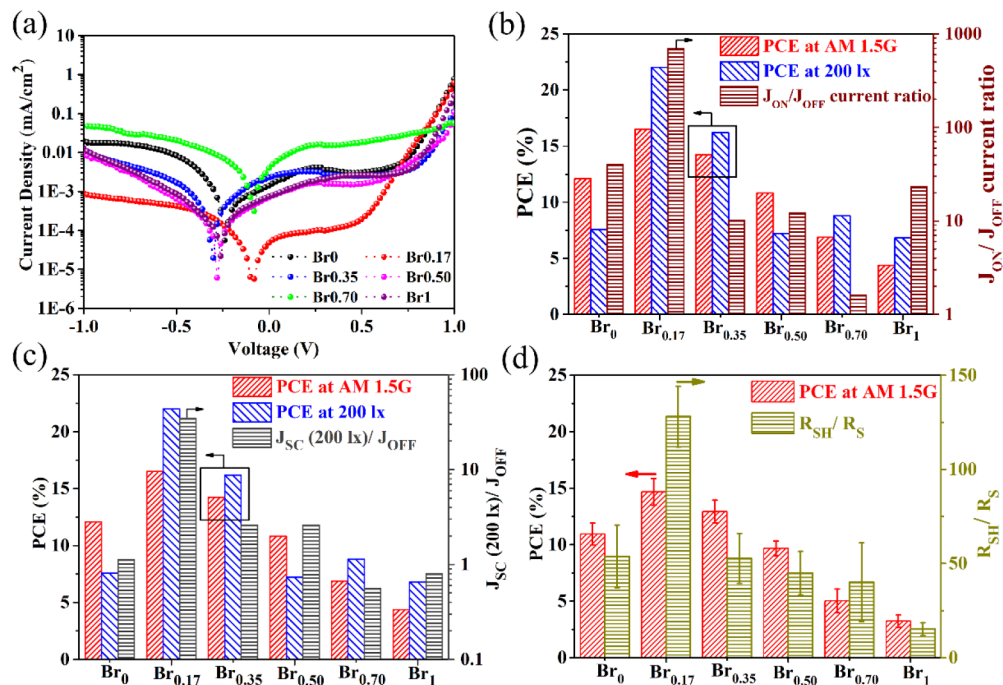
Figure 5. (a) Tafel plot of the dark current density versus voltage. (b, c) Power conversion efficiency (PCE) of the best cells measured under standard test conditions (STC, red filled bars) and under 200 lx (blue filled bars), (b) with J_{ON}/J_{OFF} current ratio extracted from dark $J-V$ measurements at +1 V (J_{ON}) and −1 V (J_{OFF}) (burgundy colored filled bars), and (c) J_{SC} (200 lx)/J_{OFF} (dark gray filled bars), where J_{SC} is the short circuit current measured at 200 lx under LED light and J_{OFF} is the dark current calculated at −1 V. (d) Average PCE (red filled bars) under STC with shunt resistance/series resistance (R_{SH}/R_S) ratios calculated from $J-V$ curves measured at STC (dark yellow filled bars).

appearing at $2\theta \approx 11.2°$ are from the non-photoactive δ_H-FAPbI$_3$ (yellow phase).[57,58]

It is apparent from Figures 6b and S8 that at 200 lx PCEs of almost all photovoltaic cells have degraded more rapidly than when measured under 1 sun with the more durable ones being those with Br0.17, Br0.35, and Br0.5 compositions that maintained ∼60% of the original PCE. For the rest, the PCE drop was of 80% or more at 200 lx. This high aging rate of the PCE measured indoors (on average the drop was 65% for all cells) compared to that at STC (41% fall over all the same cells) over time is consistent with PV performance being more sensitive to defects for the former and is in line with a previous report on a different technology, that of dye sensitized solar cells.[12] The differential aging rate we observed when measuring the cells under indoor illumination compared to under STC should give impetus in giving more attention to the stability of solar cells for indoor light harvesting in future studies.

2.5. Discussion. We have determined that grain size, grain separation, film uniformity and quality, in relation to recombination, and characteristic resistances play a major role in the performance of solar cells when varying their composition through Br integration in the perovskite semi-conductor, even more than the bandgap. Further discussion is warranted at this point. First, sub-bandgap emission for Br0.7 film, and to a lesser extent for Br0.5 film, found in the PL spectra (Figure 1d) at higher wavelengths compared to the main peak, is strongly suggestive of halide phase separation, specifically I-rich domains with narrower energy gaps.[59−62] These act as recombination centers, contributing to the poor performance of the Br0.5 and Br0.7 cells.[60,61] The fact that phase separation (also known to be reversible) is brought about by the incident light brings about further complexity in the system as reported in many references focusing specifically

on this aspect.[63−67] The dynamics are likely not affecting the main focus consisting of our indoor spot $J-V$ measurements, especially at 200 lx with low optical powers of 0.77 W/m^2 and a single scan time less than 10 s.[67] Furthermore, the noncontinuous electron beam excitation we used for SEM measurement has been shown to not induce any phase separation.[63,68] Dedicated systematic investigations of photo-induced phase separation can be found in refs 59−67. A focus of future studies could fix Br composition and vary film quality through other methods such as solvent or processing parameters to decouple the morphology from perovskite chemistry. Other future studies could narrow the Br range between 0% and 20% to pinpoint more exactly the effect of Br in a range where light-induced phase segregation is not significant.[59,62]

Going the full 0−100% range has given the opportunity to determine some general helpful parameters in the morphology, composition, defect, and optoelectronic properties space, which has led to better indoor performance. These have been summarized in Table 1. Additionally, the study has highlighted the need of strategies that can enable a better phase uniformity at high Br content, especially for indoor applications. These could rely on engineering additive compounds to be introduced in the main active materials as a way to obtain more compact perovskite films, thus bringing PCEs closer to the theoretical maximum.[8,19]

3. CONCLUSIONS

We prepared a series of perovskite absorbers [Cs$_{0.05}$(MA$_{0.17}$FA$_{0.83}$)$_{0.95}$Pb(I$_{1−x}$Br$_x$)$_3$, $0 \leq x \leq 100\%$]. We found that bandgap (E_g) is linearly related to Br$^-$ content (x): E_g/eV = 0.75x+1.48. The $J-V$ characterizations show that the PCE as a function of E_g displayed a different trend compared
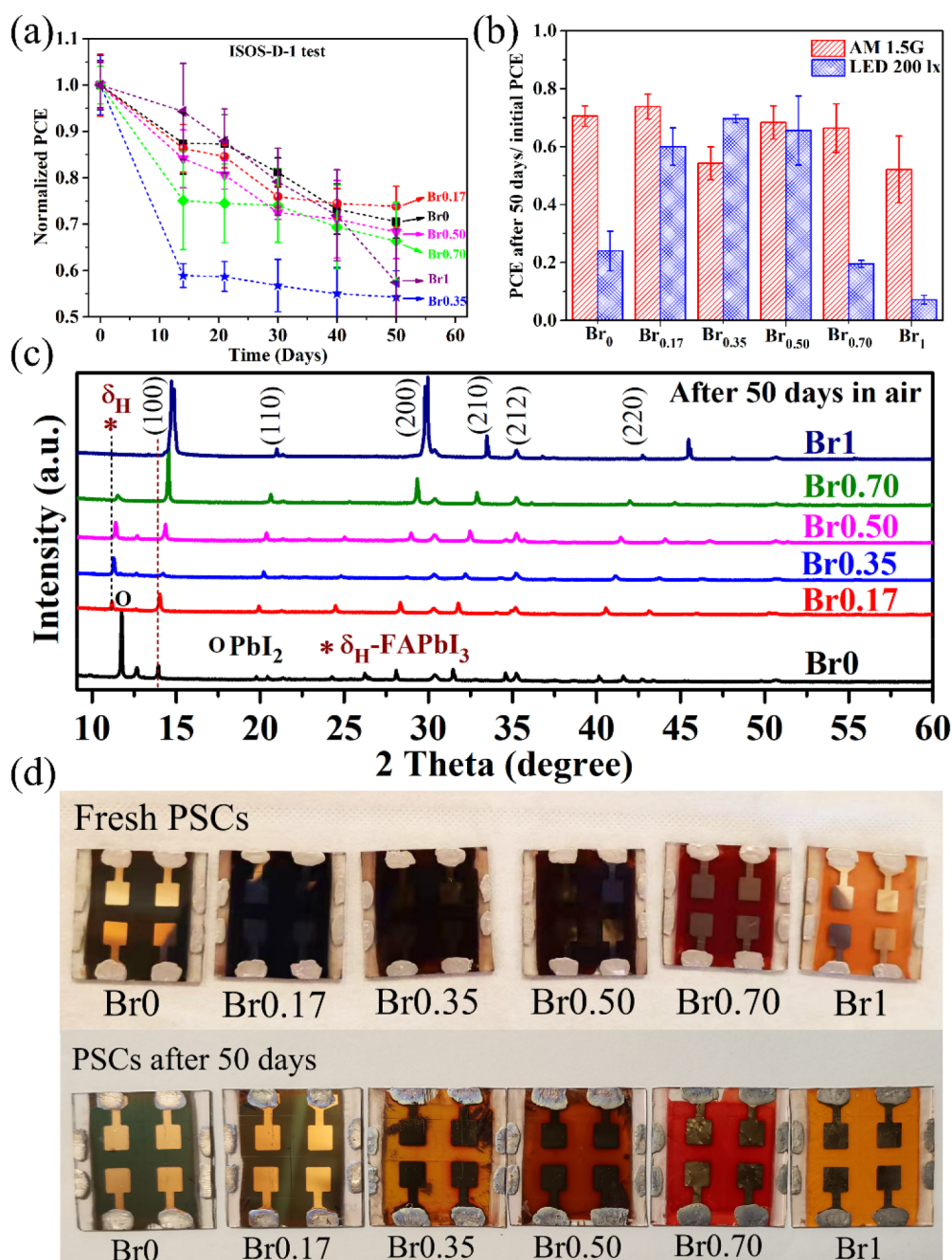
Figure 6. Long-term stability test for $Cs_{0.05}(MA_{0.17}FA_{0.83})_{0.95}Pb(I_{1-x}Br_x)_3$ $[0 \leq x \leq 100\%]$ perovskite solar cells without any encapsulation under ambient conditions in the dark. (a) Evolution of normalized PCEs of devices for measurements at standard test conditions (ISOS-D-1 test). Each average (symbol) and standard deviation (error bar) was calculated from four solar cells. (b) Ratios between the PCE of devices at day 50 and day 0 for measurements at standard test conditions (red filled bars) and at 200 lx (blue filled bars). (c) XRD patterns of perovskite films placed in air after 50 days. (d) Photographs of perovskite solar cells at day 0 (top) and day 50 (bottom).

to the theoretically maximum limits especially under indoor illumination. At Br^- content of $x = 0.17$ ($E_g = 1.61$ eV, instead of the one close to the theoretical bandgap 1.9 eV) the PCE was maximum, i.e., of 22.0% (200 lx) and 27.1% (1000 lx), under LED illumination. Thus, film quality was shown to be more important than E_g. Our investigation has enabled dentification and quantification of a number of important parameters that enable one to achieve high performance (>25% PCE at 1000 lx) at low light levels for these types of solar cells summarized in Table 1. Films with average grain sizes exceeding 300 nm (>70% of film thickness) and high

compactness with intergrain spacing ≪ 10 nm are required. Furthermore, both J_{ON}/J_{OFF} ratio (dark current densities at +1/at −1 V) and shunt/series resistance ratio (R_{SH}/R_S) should be greater than 10^2 as well as J_{SC} (200 lx)/J_{OFF} should be larger than 10. From long-term stability data, we found that the degradation rate of the PCE measured indoors was 59% larger than that at STC in relative terms due to the PV performance being more sensitive to defects for the former, and linked to grain size and intergrain spacing (i.e., grain boundary surface areas). Overall, the systematic investigation presented here has helped deepen the understanding of the difference in solar cell

efficiency and stability and of some important underlying mechanisms, when operated under indoors illumination versus standard test conditions (1 sun).

4. EXPERIMENTAL SECTION

4.1. Materials. Tin oxide (SnO_2), 15% in H_2O colloidal dispersion, was purchased from Alfa Aesar. PbI_2 and $PbBr_2$ were purchased from TCI Co. FAI, FABr, MAI, MABr, CsI, CsBr, dimethylformamide (DMF) (99.8%), dimethyl sulfoxide (DMSO) (99.5%), and chlorobenzene (99.8%) were purchased from Sigma-Aldrich. The Spiro-OMeTAD (≥99.8%) was purchased from Borun NewMaterial Technology Ltd. 4-*tert*-Butylpyridine (tBP) and bis-(trifluoromethylsulfonyl)amine lithium salt) (LiTFSI) were purchased from Sigma-Aldrich.

4.2. Device Fabrication. At first, glass/indium tin oxide (ITO) plates were patterned using a raster scanning laser.[48] Then, the prepared glass/ITO substrates (25 mm × 25 mm) were step-by-step cleaned in an ultrasonic bath using deionized water, acetone, isopropanol, and deionized water for 15 min each. Then, cleaned substrates were dried and placed under UV−ozone treatment for 15 min. For the fabrication of $ITO/SnO_2/Cs_{0.05}(MA_{0.17}FA_{0.83})_{0.95}Pb(I_{1-x}Br_x)_3$/Spiro-OMeTAD/Au devices, tin oxide (SnO_2) precursor solution was prepared by mixing SnO_2 (15% in H_2O colloidal dispersion) with deionized water (1:5, v:v), which was further stirred 2 h. Then, SnO_2 solution was spin coated on glass/ITO substrate at 2500 rpm for 30 s in air and annealed at 100 °C for 10 min in ambient air.

To the deposited $Cs_{0.05}(MA_{0.17}FA_{0.83})_{0.95}Pb(I_{1-x}Br_x)_3$ ($x = 0, 0.17, 0.35, 0.5, 0.7,$ and 1) perovskite layer, the perovskite precursor solutions with different formulas containing various ions were prepared in anhydrous DMF:DMSO (4:1, v:v) and stirred overnight at room temperature. The perovskite precursor was spin coated on the SnO_2 layer following a two steps procedure at 1000 rpm for 10 s and then at 6000 rpm for the next 20 s. 185 μL of chlorobenzene (CB) was dropped on the spinning substrate 15 s before the end of the procedure. After spinning, the substrates were immediately moved to a hot plate and then annealed at 100 °C for 10 min in a nitrogen filled glovebox. After the substrates were cooled to room temperature, then a Spiro-OMeTAD precursor solution [with recipe of Spiro-OMeTAD (72.3 mg) doped with 17.5 μL of LiTFSI solution (520 mg/mL in acetonitrile) and 28.8 μL of tBP in 1 mL of CB] was spin coated at 4000 rpm for 30 s on the perovskite layer. Finally, 100 nm of gold top electrode was deposited on the Spiro layer by thermal evaporation to complete the preparation process of the PSCs.

4.3. Characterization. The ultraviolet−visible (UV−vis) absorption spectra were charactered by UV−vis 2550 Spectrophotometer from Shimadzu. The top-view surface morphology of different Br-containing perovskite films were measured by Hitachi SU8000 scanning electron microscope (SEM). Grain size of each different Br-containing perovskite film was analyzed using the software of Nano Measurer 1.2. The thicknesses of perovskite films were measured by confocal microscope (Olympus Lext-3100). Current density−voltage ($J-V$) characterizations of the devices were by a source meter (Keithley 2400) equipped with a calibrated solar simulator (ABET Sun 2000, class A) providing standard test conditions (AM1.5G, 1000 W/m^2) at room temperature. PL, external quantum efficiency (EQE), and dark $J-V$ spectra were characterized by using a modular testing platform (Arkeo-Cicci Research s.r.l.).[10,69]

Indoor $J-V$ of PSCs were measured by a customized home-built installation; a detailed description can be found in our previous publication.[12] The installation was equipped with a white LED (Osram Parathom Classic P25) as the light source, whose emission spectrum is shown in Figure S1b. The specific illuminance (e.g., 200, 400, 500, and 1000 lx) can be obtained by changing the distance between devices and the LED light source. Prior to each characterization, the illuminance was calibrated by using a luxmeter (NIST-traceable calibrated Digisense 20250-00). For all of the $J-V$ characterizations, an active area (0.09 cm^2) of the device was defined using a black tape mask.

■ ASSOCIATED CONTENT

ⓢ Supporting Information

The Supporting Information is available free of charge at https://pubs.acs.org/doi/10.1021/acsaem.2c03394.

> Schematic device structure diagram, LED lamp irradiance, PV parameters statistics, best $J-V$ curves, perovskite film thicknesses, series (R_S) and shunt (R_{SH}) resistances, dependence of PV parameters on R_{SH}/R_S, PCEs' long-term stabilities, hysteresis index table, and on/off current and on/off current ratios summary table (PDF)

■ AUTHOR INFORMATION

Corresponding Author

  Thomas M. Brown − CHOSE (Centre for Hybrid and Organic Solar Energy), Department of Electronic Engineering, University of Rome Tor Vergata, 00133 Rome, Italy; ⊙ orcid.org/0000-0003-2141-3587; Email: thomas.brown@uniroma2.it

Authors

  Jie Xu − CHOSE (Centre for Hybrid and Organic Solar Energy), Department of Electronic Engineering, University of Rome Tor Vergata, 00133 Rome, Italy

  Suresh Kumar Podapangi − CHOSE (Centre for Hybrid and Organic Solar Energy), Department of Electronic Engineering, University of Rome Tor Vergata, 00133 Rome, Italy

  Sathy Harshavardhan Reddy − CHOSE (Centre for Hybrid and Organic Solar Energy), Department of Electronic Engineering, University of Rome Tor Vergata, 00133 Rome, Italy

  Luigi Angelo Castriotta − CHOSE (Centre for Hybrid and Organic Solar Energy), Department of Electronic Engineering, University of Rome Tor Vergata, 00133 Rome, Italy; ⊙ orcid.org/0000-0003-2525-8852

  Aldo Di Carlo − CHOSE (Centre for Hybrid and Organic Solar Energy), Department of Electronic Engineering, University of Rome Tor Vergata, 00133 Rome, Italy; Institute for Structure of Matter, National Research Council (CNR-ISM), 00133 Rome, Italy; ⊙ orcid.org/0000-0001-6828-2380

Complete contact information is available at:
https://pubs.acs.org/10.1021/acsaem.2c03394

Notes

The authors declare no competing financial interest.

■ REFERENCES

(1) Jena, A. K.; Kulkarni, A.; Miyasaka, T. Halide perovskite photovoltaics: background, status, and future prospects. *Chem. Rev.* **2019**, *119*, 3036−3103.

(2) Li, N. X.; Tao, S. X.; Chen, Y. H.; Niu, X. X.; Onwudinanti, C. K.; Hu, C.; Qiu, Z. W.; Xu, Z. Q.; Zheng, G.; Wang, L. G.; Zhang, Y.;

Li, L.; Liu, H. F.; Lun, Y. Z.; Hong, J. W.; Wang, X. Y.; Liu, Y. Q.; Xie, H. P.; Gao, Y. L.; Bai, Y.; Yang, S. H.; Brocks, G.; Chen, Q.; Zhou, H. P. Cation and anion immobilization through chemical bonding enhancement with fluorides for stable halide perovskite solar cells. *Nat. energy* **2019**, *4*, 408−415.

(3) Stranks, S. D.; Snaith, H. J. Metal-halide perovskites for photovoltaic and light-emitting devices. *Nat. nanotechnol* **2015**, *10*, 391−402.

(4) National Renewable Enery Laboratory. *Best research-cell efficiency chart*, Jan. 18, 2023. https://www.nrel.gov/pv/cell-efficiency.html.

(5) Kim, S.; Jahandar, M.; Jeong, J. H.; Lim, D. C. Recent progress in solar cell technology for low-light indoor applications. *Curr. Altern. Energy* **2019**, *3*, 3−17.

(6) Kim, S.; Oh, H.; Kang, G.; Han, I. K.; Jeong, I.; Park, M. High-Power and Flexible Indoor Solar Cells via Controlled Growth of Perovskite Using a Greener Antisolvent. *ACS Appl. Energy Mater.* **2020**, *3*, 6995−7003.

(7) Di Giacomo, F.; Fakharuddin, A.; Jose, R.; Brown, T. M. Progress, challenges and perspectives in flexible perovskite solar cells. *Energy Environ. Sci.* **2016**, *9*, 3007−3035.

(8) He, X.; Chen, J.; Ren, X.; Zhang, L.; Liu, Y. C.; Feng, J. S.; Fang, J. J.; Zhao, K.; Liu, S. Z. 40.1% Record Low-Light Solar-Cell Efficiency by Holistic Trap-Passivation using Micrometer-Thick Perovskite Film. *Adv. Mater.* **2021**, *33*, 2100770.

(9) Di Giacomo, F.; Zardetto, V.; Lucarelli, G.; Cinà, L.; Di Carlo, A.; Creatore, M.; Brown, T. M. Mesoporous perovskite solar cells and the role of nanoscale compact layers for remarkable all-round high efficiency under both indoor and outdoor illumination. *Nano Energy* **2016**, *30*, 460−469.

(10) Castro-Hermosa, S.; Lucarelli, G.; Top, M.; Fahland, M.; Fahlteich, J.; Brown, T. M. Perovskite Photovoltaics on Roll-To-Roll Coated Ultra-thin Glass as Flexible High-Efficiency Indoor Power Generators. *Cell Reports Phys. Sci.* **2020**, *1*, 100045.

(11) Mathews, I.; Kantareddy, S. N.; Buonassisi, T.; Peters, I. M. Technology and Market Perspective for Indoor Photovoltaic Cells. *Joule* **2019**, *3*, 1415−1426.

(12) De Rossi, F.; Pontecorvo, T.; Brown, T. M. Characterization of photovoltaic devices for indoor light harvesting and customization of flexible dye solar cells to deliver superior efficiency under artificial lighting. *Appl. Energy* **2015**, *156*, 413−422.

(13) Mathews, I.; Kantareddy, S. N. R.; Sun, S.; Layurova, M.; Thapa, J.; Correa-Baena, J. P.; Bhattacharyya, R.; Buonassisi, T.; Sarma, S.; Peters, I. M. Self-Powered Sensors Enabled by Wide-Bandgap Perovskite Indoor Photovoltaic Cells. *Adv. Funct. Mater.* **2019**, *29*, 1904072.

(14) Lechêne, B. P.; Cowell, M.; Pierre, A.; Evans, J. W.; Wright, P. K.; Arias, A. C. Organic solar cells and fully printed super-capacitors optimized for indoor light energy harvesting. *Nano Energy* **2016**, *26*, 631−640.

(15) Biswas, S.; Kim, H. Solar Cells for Indoor Applications: Progress and Development. *Polymers* **2020**, *12*, 1338.

(16) Li, Z.; Zhang, J.; Wu, S. F.; Deng, X.; Li, F. Z.; Liu, D. J.; Lee, C.; Lin, F.; Lei, D. Y.; Chueh, C.; Zhu, Z. L.; Jen, A. K.-Y. Minimized surface deficiency on wide-bandgap perovskite for efficient indoor photovoltaics. *Nano Energy* **2020**, *78*, 105377.

(17) Freunek, M.; Freunek, M.; Reindl, L. M. Maximum efficiencies of indoor photovoltaic devices. *IEEE J. Photovolt.* **2013**, *3*, 59−64.

(18) Hu, Z. S.; Lin, Z. H.; Su, J.; Zhang, J. C.; Chang, J. J.; Hao, Y. A review on energy band-gap engineering for perovskite photovoltaics. *Solar Rrl* **2019**, *3*, 1900304.

(19) Cheng, R.; Chung, C. C.; Zhang, H.; Liu, F. Z.; Wang, W. T.; Zhou, Z. W.; Wang, S. J.; Djurišić, A. B.; Feng, S. P. Tailoring Triple-Anion Perovskite Material for Indoor Light Harvesting with Restrained Halide Segregation and Record High Efficiency Beyond 36%. *Adv. Energy Mater.* **2019**, *9*, 1901980.

(20) Mainville, M.; Leclerc, M. Recent Progress on Indoor Organic Photovoltaics: From Molecular Design to Production Scale. *Acs Energy Lett.* **2020**, *5*, 1186−1197.

(21) Castelli, I. E.; García-Lastra, J. M.; Thygesen, K. S.; Jacobsen, K. W. Bandgap calculations and trends of organometal halide perovskites. *APL Mater.* **2014**, *2*, 081514.

(22) Brivio, F.; Caetano, C.; Walsh, A. Thermodynamic origin of photoinstability in the CH_3NH_3Pb $(I_{1-x} Br_x)_3$ hybrid halide perovskite alloy. *J. Phys. Chem. Lett.* **2016**, *7*, 1083−1087.

(23) Chen, Q.; De Marco, N.; Yang, Y.; Song, T. B.; Chen, C. C.; Zhao, H. X.; Hong, Z.; Zhou, H. P.; Yang, Y. Under the spotlight: The organic-inorganic hybrid halide perovskite for optoelectronic applications. *Nano Today* **2015**, *10*, 355−396.

(24) Wu, M. J.; Kuo, C. C.; Jhuang, L. S.; Chen, P. H.; Lai, Y. F.; Chen, F. C. Bandgap engineering enhances the performance of mixed-cation perovskite materials for indoor photovoltaic applications. *Adv. Energy Mater.* **2019**, *9*, 1901863.

(25) Saliba, M.; Matsui, T.; Seo, J.; Domanski, K.; Correa-Baena, J. P.; Nazeeruddin, M. K.; Zakeeruddin, S. M.; Tress, W.; Abate, A.; Hagfeldt, A.; Grätzel, M. Cesium-containing triple cation perovskite solar cells: improved stability, reproducibility and high efficiency. *Energy Environ. Sci.* **2016**, *9*, 1989−1997.

(26) Yang, G.; Ren, Z. W.; Liu, K.; Qin, M. C.; Deng, W. Y.; Zhang, H. K.; Wang, H. B.; Liang, J. W.; Ye, F. H.; Liang, Q.; Yin, H.; Chen, Y. X.; Zhuang, Y. L.; Li, S. Q.; Gao, B. W.; Wang, J. B.; Shi, T. T.; Wang, X.; Lu, X. H.; Wu, H. B.; Hou, J. H.; Lei, D. Y.; So, S. K.; Yang, Y.; Fang, G. J.; Li, G. Stable and low-photovoltage-loss perovskite solar cells by multifunctional passivation. *Nat. Photonics* **2021**, *15*, 681−689.

(27) Cui, D.; Yang, Z.; Yang, D.; Ren, X. D.; Liu, Y. C.; Wei, Q. B.; Fan, H. B.; Zeng, J. H.; Liu, S. Z. F. Color-tuned perovskite films prepared for efficient solar cell applications. *J. Phys. Chem. C* **2016**, *120*, 42−47.

(28) Suarez, B.; Gonzalez-Pedro, V.; Ripolles, T. S.; Sanchez, R. S.; Otero, L.; Mora-Sero, I. Recombination study of combined halides (Cl, Br, I) perovskite solar cells. *J. Phys. Chem. Lett.* **2014**, *5*, 1628−1635.

(29) Noh, J. H.; Im, S. H.; Heo, J. H.; Mandal, T. N.; Seok, S. Chemical management for colorful, efficient, and stable inorganic-organic hybrid nanostructured solar cells. *Nano Lett.* **2013**, *13*, 1764−1769.

(30) Solanki, C. S. *Solar Photovoltaics: Fundamentals, Technologies and Applications*, 3rd ed.; PHI Learning: Delhi, India, 2015; p 106

(31) Nelson, J. *The Physics of Solar Cells*; Imperial College Press: London, U.K., 2003; p 29.

(32) Son, D. Y.; Kim, S. G.; Seo, J. Y.; Lee, S. H.; Shin, H.; Lee, D.; Park, N. G. Universal approach toward hysteresis-free perovskite solar cell via defect engineering. *J. Am. Chem. Soc.* **2018**, *140*, 1358−1364.

(33) Minbashi, M.; Yazdani, E. Comprehensive study of anomalous hysteresis behavior in perovskite-based solar cells. *Sci. Rep.* **2022**, *12*, 14916.

(34) García-Rodríguez, R.; Riquelme, A. J.; Cowley, M.; Valadez-Villalobos, K.; Oskam, G.; Bennett, L. J.; Wolf, M. J.; Contreras-Bernal, L.; Cameron, P. J.; Walker, A. B.; Anta, J. A. Inverted Hysteresis in n-i-p and p-i-n Perovskite Solar Cells. *Energy Technol.* **2022**, *10*, 2200507.

(35) Bu, T.; Li, J.; Lin, Q.; McMeekin, D. P.; Sun, J.; Wang, M.; Chen, W.; Wen, X.; Mao, W.; McNeill, C. R.; et al. Structure engineering of hierarchical layered perovskite interface for efficient and stable wide bandgap photovoltaics. *Nano Energy* **2020**, *75*, 104917.

(36) Liu, L.; Yang, Y.; Du, M.; Cao, Y.; Ren, X.; Zhang, L.; Wang, H.; Zhao, S.; Wang, K.; Liu, S. Self-Assembled Amphiphilic Monolayer for Efficient and Stable Wide-Bandgap Perovskite Solar Cells. *Adv. Energy Mater.* **2023**, *13*, 2202802.

(37) Shockley, W.; Queisser, H. J. Detailed Balance Limit of Efficiency of p-n Junction Solar. *Cells. J. Appl. Phys.* **1961**, *32*, 510−519.

(38) Rühle, S. Tabulated values of the Shockley-Queisser limit for single junction solar cells. *Sol. Energy* **2016**, *130*, 139−147.

(39) Knight, A. J.; Borchert, J.; Oliver, R. D. J.; Patel, J. B.; Radaelli, P. G.; Snaith, H. J.; Johnston, M. B.; Herz, L. M. Halide Segregation

in Mixed-Halide Perovskites: Influence of A-Site Cations. *ACS Energy Lett.* **2021**, *6*, 799−808.

(40) Shen, H.; Nan, R.; Jian, Z.; Li, X. Defect step controlled growth of perovskite MAPbBr$_3$ single crystal. *J. Mater. Sci.* **2019**, *54*, 11596−11603.

(41) Ruess, R.; Benfer, F.; Böcher, F.; Stumpp, M.; Schlettwein, D. Stabilization of Organic-Inorganic Perovskite Layers by Partial Substitution of Iodide by Bromide in Methylammonium Lead Iodide. *ChemPhysChem* **2016**, *17*, 1505.

(42) García-Rodríguez, R.; Ferdani, D.; Pering, S.; Baker, P. J.; Cameron, P. J. Influence of bromide content on iodide migration in inverted MAPb(I$_{1-x}$Br$_x$)$_3$ perovskite solar cells. *J. Phys. Chem. A* **2019**, *7*, 22604−22614.

(43) Castro-Méndez, A.; Hidalgo, J.; Correa-Baena, J. The role of grain boundaries in perovskite solar cells. *Adv. Energy Mater.* **2019**, *9*, 1901489.

(44) Shao, Y.; Fang, Y.; Li, T.; Wang, Q.; Dong, Q.; Deng, Y.; Yuan, Y.; Wei, H.; Wang, M.; Gruverman, A.; Shield, J.; Huang, J. Grain boundary dominated ion migration in polycrystalline organic-inorganic halide perovskite films. *Energy Environ. Sci.* **2016**, *9*, 1752−1759.

(45) Dkhili, M.; Lucarelli, G.; De Rossi, F.; Taheri, B.; Hammedi, K.; Ezzaouia, H.; Brunetti, F.; Brown, T. M. Attributes of High-Performance Electron Transport Layers for Perovskite Solar Cells on Flexible PET versus on Glass. *ACS Appl. Energy Mater.* **2022**, *5*, 4096−4107.

(46) Sheng, W. P.; Yang, J.; Li, X.; Liu, G. L.; Lin, Z. J.; Long, J.; Xiao, S. Q.; Tan, L. C.; Chen, Y. W. Tremendously enhanced photocurrent enabled by triplet-triplet annihilation up-conversion for high-performance perovskite solar cells. *Energy Environ. Sci.* **2021**, *14*, 3532−3541.

(47) Lucarelli, G.; Di Giacomo, F.; Zardetto, V.; Creatore, M.; Brown, T. M. Efficient light harvesting from flexible perovskite solar cells under indoor white light-emitting diode illumination. *Nano Res.* **2017**, *10*, 2130−2145.

(48) Dagar, J.; Castro-Hermosa, S.; Lucarelli, G.; Zampetti, A.; Cacialli, F.; Brown, T. M. Low-temperature solution-processed thin SnO$_2$/Al$_2$O$_3$ double electron transport layers toward 20% efficient perovskite solar cells. *IEEE J. Photovolt.* **2019**, *9*, 1309−1315.

(49) Wetzelaer, G. A. H.; Scheepers, M.; Sempere, A. M.; Momblona, C.; Ávila, J.; Bolink, H. J. Trap-assisted non-radiative recombination in organic-inorganic perovskite solar cells. *Adv. Mater.* **2015**, *27*, 1837−1841.

(50) Taheri, B.; De Rossi, F.; Lucarelli, G.; Castriotta, L. A.; Di Carlo, A.; Brown, T. M.; Brunetti, F. Laser-Scribing Optimization for Sprayed SnO$_2$-Based Perovskite Solar Modules on Flexible Plastic Substrates. *ACS Appl. Energy Mater.* **2021**, *4*, 4507−4518.

(51) Dagar, J.; Castro-Hermosa, S.; Gasbarri, M.; Palma, A. L.; Cina, L.; Matteocci, F.; Calabrò, E.; Di Carlo, A.; Brown, T. M. Efficient fully laser-patterned flexible perovskite modules and solar cells based on low-temperature solution-processed SnO$_2$/mesoporous-TiO$_2$ electron transport layers. *Nano Res.* **2018**, *11*, 2669−2681.

(52) Reese, M. O.; Gevorgyan, S. A.; Jørgensen, M.; Bundgaard, E.; Kurtz, S. R.; Ginley, D. S.; Olson, D. C.; Lloyd, M. T.; Morvillo, P.; Katz, E. A.; et al. Consensus stability testing protocols for organic photovoltaic materials and devices. *Sol. Energy Mater. Sol. Cells* **2011**, *95*, 1253−1267.

(53) Khenkin, M. V.; Katz, E. A.; Abate, A.; Bardizza, G.; Berry, J. J.; Brabec, C.; Brunetti, F.; Bulović, V.; Burlingame, Q.; Di Carlo, A.; et al. Consensus statement for stability assessment and reporting for perovskite photovoltaics based on ISOS procedures. *Nat. Energy* **2020**, *5*, 35−49.

(54) Chiang, C. H.; Wu, C. G. Film grain-size related long-term stability of inverted perovskite solar cells. *ChemSusChem* **2016**, *9*, 2666−2672.

(55) Song, T. B.; Yokoyama, T.; Stoumpos, C. C.; Logsdon, J.; Cao, D. H.; Wasielewski, M. R.; Aramaki, S.; Kanatzidis, M. G. Importance of reducing vapor atmosphere in the fabrication of tin-based perovskite solar cells. *J. Am. Chem. Soc.* **2017**, *139*, 836−842.

(56) Li, Z.; Yang, M.; Park, J. S.; Wei, S. H.; Berry, J. J.; Zhu, K. Stabilizing Perovskite Structures by Tuning Tolerance Factor: Formation of Formamidinium and Cesium Lead Iodide Solid-State Alloys. *Chem. Mater.* **2016**, *28*, 284−292.

(57) Liu, T.; Lai, H.; Wan, X.; Zhang, X.; Liu, Y.; Chen, Y. Cesium Halides-Assisted Crystal Growth of Perovskite Films for Efficient Planar Heterojunction Solar Cells. *Chem. Mater.* **2018**, *30*, 5264−5271.

(58) Zarabinia, N.; Lucarelli, G.; Rasuli, R.; De Rossi, F.; Taheri, B.; Javanbakht, H.; Brunetti, F.; Brown, T. M. Simple and effective deposition method for solar cell perovskite films using a sheet of paper. *iScience* **2022**, *25*, 103712.

(59) Hoke, E. T.; Slotcavage, D. J.; Dohner, E. R.; Bowring, A. R.; Karunadasa, H. I.; McGehee, M. D. Reversible photo-induced trap formation in mixed-halide hybrid perovskites for photovoltaics. *Chem. Sci.* **2015**, *6*, 613−617.

(60) Barker, A. J.; Sadhanala, A.; Deschler, F.; Gandini, M.; Senanayak, S. P.; Pearce, P. M.; Mosconi, E.; Pearson, A. J.; Wu, Y.; Srimath Kandada, A. R.; Leijtens, T.; De Angelis, F.; Dutton, S. E.; Petrozza, A.; Friend, R. H. Defect-assisted photoinduced halide segregation in mixed-halide perovskite thin films. *ACS Energy Lett.* **2017**, *2*, 1416−1424.

(61) Motti, S. G.; Patel, J. B.; Oliver, R. D. J.; Snaith, H. J.; Johnston, M. B.; Herz, L. M. Phase segregation in mixed-halide perovskites affects charge-carrier dynamics while preserving mobility. *Nat. Commun.* **2021**, *12*, 6955.

(62) Diez-Cabanes, V.; Even, J.; Beljonne, D.; Quarti, C. Electronic structure and optical properties of mixed iodine/bromine lead perovskites. To mix or not to mix. *Adv. Opt. Mater.* **2021**, *9*, 2001832.

(63) Bischak, C. G.; Hetherington, C. L.; Wu, H.; Aloni, S.; Ogletree, D. F.; Limmer, D. T.; Ginsberg, N. S. Origin of reversible photoinduced phase separation in hybrid perovskites. *Nano Lett.* **2017**, *17*, 1028−1033.

(64) Beal, R. E.; Hagström, N. Z.; Barrier, J.; Gold-Parker, A.; Prasanna, R.; Bush, K. A.; Passarello, D.; Schelhas, L. T.; Brüning, K.; Tassone, C. J.; et al. Structural Origins of Light-Induced Phase Segregation in Organic-Inorganic Halide Perovskite Photovoltaic Materials. *Matter* **2020**, *2*, 207−219.

(65) Kuno, M.; Brennan, M. C. What exactly causes light-induced halide segregation in mixed-halide perovskites? *Matter* **2020**, *2*, 21−23.

(66) Guo, Y.; Yin, X.; Liu, D.; Liu, J.; Zhang, C.; Xie, H.; Yang, Y.; Que, W. Photoinduced self-healing of halide segregation in mixed-halide perovskites. *ACS Energy Lett.* **2021**, *6*, 2502−2511.

(67) Draguta, S.; Sharia, O.; Yoon, S. J.; Brennan, M. C.; Morozov, Y. V.; Manser, J. S.; Kamat, P. V.; Schneider, W. F.; Kuno, M. Rationalizing the light-induced phase separation of mixed halide organic-inorganic perovskites. *Nat. Commun.* **2017**, *8*, 200−8.

(68) Yang, X.; Yan, X.; Wang, W.; Zhu, X.; Li, H.; Ma, W.; Sheng, C. Light induced metastable modification of optical properties in CH$_3$NH$_3$PbI$_{3-x}$Br$_x$ perovskite films: Two-step mechanism. *Org. Electron.* **2016**, *34*, 79−83.

(69) Dagar, J.; Castro-Hermosa, S.; Lucarelli, G.; Cacialli, F.; Brown, T. M. Highly efficient perovskite solar cells for light harvesting under indoor illumination via solution processed SnO$_2$/MgO composite electron transport layers. *Nano Energy* **2018**, *49*, 290−299.